Compliant Intracortical Implants Reduce Strains and Strain Rates in Brain Tissue *In Vivo*

Arati Sridharan[1], **Jessica K. Nguyen**[2,3], **Jeffrey R. Capadona**[2,3], and **Jit Muthuswamy**[1]

[1]School of Biological & Health Systems Engineering, Ira A. Fulton School of Engineering, Arizona State University, Tempe, AZ 85287

[2]Department of Biomedical Engineering, Case Western Reserve University, 2071 Martin Luther King Jr. Drive, Wickenden Bldg, Cleveland, OH 44106, USA

[3]Advanced Platform Technology Center, Louis Stokes Cleveland VA Medical Center, 10701 East Blvd Mail Stop 151 AW/APT, Cleveland, OH 44106-1702, USA

Abstract

Objective—The objective of this research is to characterize the mechanical interactions of (1) soft, compliant and (2) non-compliant implants with the surrounding brain tissue in a rodent brain. Understanding such interactions will enable the engineering of novel materials that will improve stability and reliability of brain implants.

Approach—Acute force measurements were made using a load cell in n=3 live rats, each with 4 craniotomies. Using an indentation method, brain tissue was tested for changes in force using established protocols. A total of 4 non-compliant, bare silicon microshanks, 3 non-compliant polyvinyl acetate (PVAc)-coated silicon microshanks, and 6 compliant, nanocomposite microshanks were tested. Stress values were calculated by dividing the force by surface area and strain was estimated using a linear stress-strain relationship. Micromotion effects from breathing and vascular pulsatility on tissue stress were estimated from a 5 sec interval of steady-state measurements. Viscoelastic properties were estimated using a second-order Prony series expansion of stress-displacement curves for each shank.

Main results—The distribution of strain values imposed on brain tissue for both compliant nanocomposite microshanks and PVAc-coated, non-compliant silicon microshanks were significantly lower compared to non-compliant bare silicon shanks. Interestingly, step-indentation experiments also showed that compliant, nanocomposite materials significantly decreased stress relaxation rates in the brain tissue at the interface ($p<0.05$) compared to non-compliant silicon and PVAc-coated silicon materials. Further, both PVAc-coated non-compliant silicon and compliant nanocomposite shanks showed significantly reduced (by 4–5 fold) stresses due to tissue micromotion at the interface.

Significance—The results of this study showed that soft, adaptive materials reduce strains and strain rates and micromotion induced stresses in the surrounding brain tissue. Understanding the material behavior at the site of tissue contact will help to improve neural implant design.

Address for future correspondence: Jit Muthuswamy, Associate Professor, SBHSE ECG 335, P.O. Box 879709, Arizona State University Tempe, AZ 85287-9709, Ph: (480) 965 1599, (jit@asu.edu).

Author Manuscript

Author Manuscript

Author Manuscript

Author Manuscript

INTRODUCTION

Intracortical microelectrodes are used typically to record the electrical activity of individual or ensembles of neurons [1, 2]. Neuroscientists implant microelectrodes into both healthy and diseased animal models to gain an understanding of neuronal connectivity and the progression of neurodegenerative diseases [3–6]. Microelectrodes can also be used as the biotic-abiotic interface for brain computer interfaces in rehabilitative applications [7–10]. Unfortunately, intracortical microelectrode technology is limited by the inability to record high-quality signals reliably over time [11–13].

Increasing evidence suggests a dominant role of neuroinflammatory events in mediating mechanical, material and biological failure modes in intracortical microelectrodes [14–16]. Several groups have suggested a major role of microglia and infiltrating blood derived macrophages in mediating neuroinflammatory events following microelectrode implantation, due to many stimulating factors [17–20]. A leading hypothesis also revolves around the mechanical mismatch surrounding implanted devices [21, 22]. Studies suggest that micromotion and tethering forces can cause damage of neural tissue surrounding implants [17, 23, 24]. For example, cortical tissue in the rat brain can displace 2–4 μm due to vascular pulsation and 10–30 μm due to breathing [25]. Self-propagation of either the cortical tissue or endothelial barrier damage can exacerbate the foreign body response to the microelectrodes and prevent wound healing events [26, 27]. Additionally, *in silico* studies have predicted that non-compliant microelectrodes composed of high modulus materials induce strain on the surrounding soft brain tissue while materials more closely matching the brain modulus significantly reduced strain on surrounding tissue [28]. *In vitro* studies have also indicated that induced strain can cause activation of pro-inflammatory pathways [29, 30]. Recently, Moshayedi *et al.* showed that CNS glial cells become activated and release pro-inflammatory molecules in response to stiff substrates [31]. Therefore, substantial efforts from several groups have gone into the development of techniques to minimize both device micromotion and the mechanical mismatch between non-compliant implants and compliant brain tissue [32–38]. Multiple groups, including the Capadona group, have demonstrated decreased neuroinflammatory responses to compliant implants [39–43]. However, experimental evidence confirming that compliant microelectrodes reduce strain and micromotion induced forces in brain tissue *in vivo* is lacking.

A recently reported method from our group measures the mechanical properties of the biotic component of the brain-electrode interface, surrounding non-compliant stainless steel microelectrode implants [44]. Specifically, we found that the estimated elastic modulus in the surrounding brain tissue fluctuates and evolves over implantation time ranging from a median value of 7.5 kPa on day 1 to 35.2 kPa after 4 weeks, indicating a progressively increasing stiffness in the brain tissue at the microelectrode-tissue interface likely due to ongoing repair and inflammatory responses in the brain tissue. Beyond 4 weeks, the estimated elastic modulus of the surrounding tissue decreases to median value of 19.6 kPa. The estimated shear modulus decreases from 28.7 kPa (4 weeks) to 7.9 kPa at 6–8 weeks, suggesting replacement or compaction of the stiffer tissue at the interface [44]. Mechanical stresses due to tissue micromotion are also reported to change significantly with implantation time along with the dynamic material property changes in brain tissue. Typical

micromotion induced effective stress amplitudes range from 0.2–0.4 kPa at day 1 of implantation to 2.6 kPa observed 4 weeks after implantation and decreasing to 0.07–0.29 kPa beyond 6 weeks of implantation (comparable to stress levels at day 1). Considering the continuously active imposition of mechanical stress on the tissue due to the mechanical mismatch between the implant and brain tissue, development of mechanically compliant substrates and coatings that also have the ability to absorb micromotion-induced stresses may mitigate the severity of scarring around the microelectrode. In this current study, we utilized the above reported novel method for mechanical characterization of brain tissue [44] to carefully assess, for the first time the mechanical stresses and strains induced in the brain tissue at the interface of a novel compliant, nanocomposite implant developed by our collaborator (Capadona lab) [45]. We then performed a quantitative comparison of the above mechanical stresses and strains with two conventional non-compliant shanks – a silicon shank and a polymer-coated silicon shank, to control for the difference in the surface chemistries of the implants.

2. MATERIALS & METHODS

2.1 Electrode fabrication & characterization

For *in vivo* experiments, three different implants were used: (1) bare silicon implants (non-compliant); (2) poly(vinyl acetate)-coated (PVAc) silicon implants (PVAc-coated non-compliant); and (3) mechanically-adaptive poly(vinyl acetate)/tunicate cellulose nanocrystal (tCNC) nanocomposites (compliant) implants, which become compliant after implantation. Single shank "Michigan" type silicon probes (1) were fabricated to a thickness of 15 μm, a length of 2 mm, and a shank width of 123 μm. PVAc-coated silicon implants (2) were created by dip-coating silicon implants in a solution of PVAc in hot toluene (10% w/w at 70°C). Implants were dipped in succession twice, allowed to dry for 30 minutes to deposit a PVAc surface layer with a thickness of ~15 +/− 5 μm [42]. Compliant implants (3) were created by casting films from a solution of PVAc and tCNC in dimethylformamide, as previously reported [45, 46]. The nanocomposite had a tCNC content of 15% w/w. The resulting films were custom molded between sheets in a hot press (Carver, Wabash, IN). Complaint implants were then fabricated by laser-micromachining with a direct-write CO_2 laser (VLS 3.5, VersaLaser) to a thickness of ~127 μm, a length of 2 mm, and a shank width of 130–140 μm [47]. All implants were ethylene oxide sterilized.

2.2 Animal surgery and force measurements

All animal procedures were carried out with the approval of the Institute of Animal Care and Use Committee (IACUC) of Arizona State University, Tempe. The experiments were performed in accordance with the National Institute of Health (NIH) guide for the care and use of laboratory animals (1996). All efforts were made to minimize animal suffering and to use only the number of animals necessary to produce reliable scientific data. The adult Sprague-Dawley rats (250–300 g) were induced using a mixture of (50 mg/ml) ketamine, (5 mg/ml) xylazine, and (1 mg/ml) acepromazine administered intramuscularly with an initial dosage of 0.1 ml/100 g body weight. The maintenance dose contained a mixture of 50 mg/ml ketamine and 5 mg/ml xylazine. Updates were given at a dose of 0.05 ml/100 g body weight based on the toe-pinch test. The rat was attached to a stereotaxic frame (Kopf

Instruments, Tujunga, CA, USA). After the skull was exposed, 4 craniotomies (~2.0 mm diameter) were drilled for the microelectrode probes with (a) 2 center points being 2.5 mm lateral and medial to the midline and 3 mm posterior to the bregma and (b) 2 center points being 2.5 mm lateral and medial to midline and 5.0 mm posterior to the bregma (Fig.1a, b). After the bone chips were carefully removed with a micro-dissection scissor, the dura was carefully incised to allow for microelectrode insertion with minimal disturbance to the observed vasculature (Fig.1c). All craniotomies were made prior to the force measurement and the exposed brain tissue was hydrated with 0.9% saline and maintained free of debris by keeping it covered with wet gelfoam. The probe-shanks were pre-mounted onto the load cell and inserted into the brain at a rate of 100 μm/s using a FHC Microdrive (Bowdoin, ME). The microelectrode probe was implanted to a depth of 1 mm in the cortex for all experiments and subsequently moved an additional 0.5 mm after 30 min. Forces experienced by the microelectrode during the insertion/penetration process were monitored using a precision load cell.

2.3. Force Measurement

Dynamic and equilibrium forces on selected microelectrode shank-probes were measured *in vivo* in adult Sprague-Dawley rats (250–300 g) using a 10g load cell (Futek, LSB210, Irvine, CA). A total of 3 rats were used for all acute measurements. To test individual microshank indentation and force response, a total of 4 craniotomies for each rat were made. Force measurements for bare silicon (Si-bare) (n=4), PVAc-coated silicon (n=3), and nanocomposite (n=6) shanks were tested in randomized order with each craniotomy used for a single shank, with the exception of two bare silicon shanks that shared the same craniotomy but the measurements were spaced at 2.0 mm apart. Microelectrode shanks were glued onto a custom mount with Loctite™ control gel super glue. Forces on the microelectrode were measured during the following sequence of steps – 1) implant microelectrodes to 1 mm depth at 100 μm/sec (phase 1), 2) hold microelectrode in place for 30 min to reach equilibrium, 3) move the microelectrode a further 0.5 mm down at 100 μm/sec (phase 2). Forces were typically registered as negative values by the load cell due to compression and tissue resistance during movement of the microelectrode into the brain. Force measurements were sampled at a frequency of 54 Hz.

In this study, we utilized a loading rate of 100 μm/sec for consistent dynamic force measurements from small dimension (~100 μm diameter) nanocomposite shanks. To test whether compliant nanocomposite shanks withstand force-indentation test methodology, nanocomposite shanks were tested using the same protocol in 0.5% (w/v) agarose gels (elastic modulus of ~8 kPa). Agarose gels have been extensively used in literature as mimics of brain tissue [48]. The force curve of a compliant nanocomposite microelectrode as it penetrates a 0.5% agarose gel mimic at 100 μm/sec is shown in Fig.2. Based on the test protocol, the nanocomposite shank is held stationary for 30 min prior to further movement in phase 2. The force curve during movement of the nanocomposite shank over a further 500 μm in depth at 100 μm/sec is also shown. The endpoint forces at 1 mm obtained using 10 μm/sec were 500–800 μN compared to 1500–2500 μN at 100 μm/sec. Agarose based gels were used to study if the nanocomposites 1) can penetrate brain like materials and 2) if the electrodes bent inside the gel after hydration. Additional tests showed that the force curves

obtained from 100 μm/sec movement protocols were more consistent compared to the 10 μm/sec, especially after penetration (data not shown). Forces on the nanocomposite microelectrode exhibited less sample-to-sample variability, especially in the relaxation process, using the 100 μm/sec penetration speed (data not shown). Nanocomposite microelectrodes were also able to penetrate without bending in the gel and remained intact after removal from gel, suggesting that a softened and more compliant microelectrode shank maintains shape and form during the indentation test and after 30–45 min exposure to hydrated brain-like conditions.

2.4 Estimation of stress and strain from force measurements

To estimate the effective stress on the microelectrode as a force per unit contact area, the contact areas of the microelectrodes in brain tissue were estimated for each individual shank geometry using SolidWorks™ (Fig.3). Since the loading rate was constant, the change in effective surface area could be calculated for each point in the force-displacement curve based on the sampling frequency of the load cell. To further calculate the effective stress on the microelectrode, the measured force was divided by the area calculated at the corresponding time point. Effective strain was calculated using a linear model:

$$\sigma = E\varepsilon \quad (1)$$

where σ is effective stress, ε represents effective strain, and E is brain tissue elastic modulus taken to be 7.5 kPa based on previous studies [44]. Maximum strain is expected to occur at a depth of 200–300 μm in the tissue, which correspond to previous observations of dimpling and points of penetration into the tissue [44]. Since motional artifacts and surface variations due to local vasculature are expected to contribute to noise in dynamic strain measurements (Fig.5), significance was assessed using an α of 0.1 for these measurements.

2.5 Analysis of Viscoelastic Parameters and Estimating Shear Moduli

After termination of movement, the forces on the microelectrode relax in a time-dependent, viscoelastic manner. The stress relaxation curves at 1 mm and 1.5 mm tissue depth (Fig.6) could be treated as a small, stepped strain experiment and characterized using conventional viscoelastic models to characterize the shear stresses on the microelectrode. The geometry of the microelectrode shanks and the fact that relaxation force measurements were done after a period of rest makes it more likely that the shear deformations were dominant during the stress-relaxation curves. However, it is likely that there are also some tensile and bulk compression/dilation around the probe. Effective stresses were calculated using the terminal depth achieved by the microelectrode (Table 1). The relaxation stress curves were smoothed using moving average method to remove effects of tissue micromotion. Due to small strains involved in the relaxation phase, a viscoelastic model described by a relaxation modulus with a 2nd order Prony series expansion was found to be the best fit ($R^2 > 0.95$):

$$G(t) = G_l + G_1 e^{-t/\tau_1} + G_2 e^{-t/\tau_2} \quad (2)$$

where $G(t)$ is the relaxation modulus as a function of time, G_l is the long term shear modulus calculated 100 sec after termination of microelectrode movement, G_1 and G_2 represent the parametric constants describing the prony series expansion, and τ_1 and τ_2 are the

characteristic short and long term time constant respectively for the tissue. This model with a Maxwell type element was also extensively described by Gefen *et al* [49]. The instantaneous shear modulus was calculated at t = 0, using

$$G(0) = G_1 + G_2 + G_{l\backslash} \quad (3)$$

Statistical means and standard error (SE) were determined excluding outliers and plotted as mean ± SE for G(0), τ_1 and τ_2. Significance was assessed using one way ANOVA for G(0), τ_1 and τ_2 values, with an α criterion of 0.05. Student's t-test was used to assess significance between individual groups for τ_1, with an α criterion of 0.05 in Fig. 7.

2.6 Analysis of stresses due to brain micromotion

To characterize the amplitude of periodic stress variations due to tissue micromotion which correlated with breathing and vascular pulsatility, the average peak-to-peak force amplitudes was determined over a 5 sec interval during steady-state (typically >100 sec after terminating microelectrode movement) of the relaxation phase. Tukey-box plots of average stresses due to micromotion in each case were plotted to determine any outliers as marked by a red dot on relevant figures. Outliers were determined as values that exceed 1.5 times the inter-quartile distance (25% and 75% percentile markers). Student's *t*-tests with an α criterion of 0.05 was used to compare stresses due to tissue micromotion between any two of the following three groups – non-compliant, bare silicon shanks (n=4), non-compliant, PVAc-coated silicon shanks (n=3), and compliant nanocomposite shanks (n=6).

3. RESULTS

3.1 Comparison of forces exerted by non-compliant and compliant shanks at the brain-implant interface

Average force-displacement curves with standard deviation (gray) during penetration of tissue as the microelectrode moves 1 mm down into the tissue (in phase 1) at 100 μm/sec are shown in Fig. 4a–c. Subsequent 0.5 mm downward movement (in phase 2) at 100 μm/sec after a 30 min wait are shown in Fig. 4d–f for bare silicon, PVAc-coated silicon, and nanocomposite shanks. In all, n=4 pairs (corresponding to phases 1 & 2) of force curves for bare-silicon shanks, n=3 pairs for PVAc-coated silicon shanks, and n=6 pairs for compliant nanocomposites in three different animals are measured. The initial portions of the force curves in Fig.4a–c (corresponding to initial displacements of 200–600 μm) reflect the dimpling/compression of the brain tissue against the electrode before penetration. After the shank is stopped at a depth of 1 mm, mainly shear relaxation forces dominate till a steady state is reached corresponding to a full relaxation of brain tissue around the shank. The steady-state forces of ~200–500 μN after relaxation were comparable in all 3 types of microelectrodes.

The range of maximum forces at a depth of 1 mm for non-compliant, bare silicon shanks are 600–1200 μN (Fig. 4a). After zeroing the starting point of force curves corresponding to phase 2, the range of maximum forces at 1.5 mm depth ranged from 600–1750 μN. For non-compliant, PVAc-coated silicon shanks, the range of maximum forces at the end of phase 1, at a depth of 1 mm, was 300–500 μN, which is smaller than those of the bare silicon

samples. At a depth of 1.5 mm, maximum forces ranged from 200–1700 μN for the PVAc-coated silicon shanks. Fig.4c & f shows the force curves generated by the compliant nanocomposite shank during phases 1 and 2. Due to the temporal changes in the effective elastic modulus of the nanocomposite material, variability was higher in the observed force curves. The range of maximum forces at a depth of 1 mm was 500–3000 μN and that corresponding to a depth of 1.5 mm was 200–2500 μN with an outlier at 10000 μN (data not shown). It is possible that the outlier shank sample might have touched against an underlying vasculature.

The force curves for the compliant nanocomposite shanks before ('stiff' state) and after hydration ('soft' state) are shown in Fig.4c & f respectively. The main difference between the 'stiff' state and the 'soft' state is observed in the relaxation curves where curves corresponding to the 'stiff' state electrodes were generally faster to relax and those corresponding to the 'soft' state generally took longer to relax.

3.2 Coated, non-compliant and compliant shanks impose less strain at brain-implant interface

Estimated dynamic stresses were calculated based on surface areas derived from CAD-based geometric models for shanks made of non-compliant, bare silicon, PVAc-coated, non-compliant silicon, and compliant nanocomposites. The CAD based models are used to derive tissue contact surface areas at any given depth (Fig.3) and a comparison of contact surface areas at a depth of 1.0 mm & 1.5 mm inside the brain tissue for each of the shanks is shown in Table 1. The nanocomposite shanks have ~98% more surface area than that of bare silicon and the PVAc-coated silicon surface areas are ~45% more than that of bare silicon at a depth of 1.0 mm. Changes in surface area account for swelling of nanocomposite material under hydration conditions at 1.5 mm. The dynamic stresses in cortical tissue induced by bare silicon, PVAc-coated silicon, and compliant nanocomposite shanks during their movement from 1.0–1.5 mm (phase 2) are shown in Fig. 5a. Penetration stresses and stresses from meningeal layers are not expected to be dominant during this phase.

A linear approximation is used to estimate dynamic strain at 200 μm tissue depth. The rationale to use strain as a point of comparison at 200 μm tissue depth is based on prior experimental observations and mechanical modeling which show that microelectrode movement beyond this depth is typically characterized by tissue tearing and shear forces beginning to dominate the observed forces [44]. Therefore, maximum tissue strain is expected to occur at this depth. Tukey-box plots show the estimated strain at 200 μm tissue depth for non-compliant, bare silicon (n=4 shanks), PVAc-coated non-compliant silicon (n=3 shanks), and compliant nanocomposite shanks (n=6 shanks) in Fig. 5b. The range of strain values was 0.10 – 0.44 for bare silicon, 0.03 – 0.26 for PVAc-coated silicon, and 0.01 – 0.21 for compliant nanocomposite excluding an outlier (0.45). The distribution of strain values show that 75% of the strain values corresponding to PVAc-coated silicon and nanocomposite shanks are below the median strain value for non-compliant, bare silicon shanks with one outlier seen for nanocomposite shanks. Strain values for non-compliant, bare silicon (n=4 shanks) were significantly different from compliant nanocomposites (n=6

shanks) ($p<0.09$). Variability in strain values corresponding to each shank type are likely due to variations in local vasculature and modulations due to related tissue micromotion.

3.3 Compliant shanks slow interfacial brain-tissue relaxation properties

After stopping movement of the electrode at 1.0 mm and 1.5 mm depth, the brain tissue undergoes a relaxation process that is reflected in the measured forces (Fig.4). The corresponding effective relaxation stresses were determined using estimated surface areas reported in Table 1. Representative relaxation curves for non-compliant, bare silicon, PVAc-coated non-compliant silicon, and compliant nanocomposite shanks are plotted in Fig.6. At t=0, the brain tissue begins to relax exponentially over time after the shanks reach cortical tissue depths of either 1 mm or 1.5 mm. For non-compliant, bare silicon shanks (Fig.6a,d), the family of relaxation force curves at a depth of 1.0 mm is similar in characteristics to the one at a depth of 1.5 mm. The relaxation force curves for PVAc-coated silicon shanks are shown in Fig.6b and 6e corresponding to depths of 1 mm and 1.5 mm respectively. The initial stresses at t=0 are the least in value for PVAc-coated silicon shanks compared using student's t-test with bonferroni correction to both bare silicon and compliant nanocomposite samples ($p<0.01$). The relaxation force curves for nanocomposite samples are shown in Fig. 6c and 6f corresponding to depths of 1 mm and 1.5 mm respectively.

To better quantitate the relaxation characteristics, a Maxwell type model with a 2nd order Prony series expansion (equation 2) was used to fit the relaxation force curves for all shanks. Viscoelastic parameters determined using the above model under step indentation-like conditions have been previously shown to be consistent with brain tissue material properties [44]. Instantaneous shear moduli calculations based on equation 3 showed no significant differences among measurements made by the different shanks as shown in Fig.7a. All the average shear modulus values (1.2–3.5 kPa) were within the same range of values as previously reported [44], confirming the consistency in material properties of the brain tissue surrounding the shanks of different materials. However, the characteristic short-term time constant (τ_1) for compliant nanocomposite shanks was significantly smaller ($p<0.05$) for relaxation force measurements at a depth of 1.0 mm (2.2 ± 2.1 sec) compared to that at a depth of 1.5 mm (5.6 ± 2.0 sec), suggesting that softened interfaces slow the rate at which brain tissue relaxes (Fig.7b). The short-term time constants for non-compliant, bare silicon shanks (4.7 ± 1.5 sec at 1.0 mm and 3.0 ± 2.0 sec at 1.5 mm) and PVAc-coated silicon shanks (2.5 ± 3.5 sec at 1.0 mm and 2.6 ± 0.9 sec at 1.5 mm) show no significant differences between relaxation forces at depths of 1 mm and 1.5 mm. However, the mean short-term relaxation (τ_1) is significantly ($p<0.05$) smaller for PVAc-coated silicon shanks compared to that of nanocomposites at 1.5 mm depth suggesting that the interaction between the softened nanocomposite and brain tissue leads to a slower rate of relaxation in stress. No significant differences are seen in the long-term time constants (τ_2) for all shanks, which ranged from 52.6–95.5 sec based on one way ANOVA. (Fig.7c)

3.4 Coated, non-compliant and compliant shanks minimize mechanical stresses due to tissue micromotion at the interface

Tissue micromotion induced stresses were observed in all types of shanks under steady-state conditions. Tissue micromotion due to breathing and heart rate pulsatility imposed a

periodic, dynamic stress on the shank. Fig.8 shows the distribution of micromotion induced stress amplitudes for non-compliant, bare silicon (n=4 measurements for each depth), PVAc-coated, non-compliant silicon (n=3 measurements for each depth), and compliant, nanocomposite shanks (n=6 measurements for each depth). The distribution of stresses (and corresponding strains) at depths of 1.0 mm and 1.5 mm are shown for each shank as Tukey-Box plots in Fig.8. The average micromotion induced stress amplitudes for non-compliant, bare silicon were significantly larger (221.5 ± 27.8 Pa at 1.0 mm and 170.6 ± 52.9 Pa at 1.5 mm) compared to those of either PVAc-coated silicon (82.2 ± 15.0 Pa at 1.0 mm and 68.3 ± 27.2 Pa at 1.5 mm) or compliant nanocomposite shanks (99.1 ± 44.3 Pa at 1.0 mm and 49.8 ± 13.4 Pa at 1.5 mm). The changing mechanical properties of 'stiff' nanocomposite before hydration at a depth of 1.0 mm compared to 'soft' and compliant states after hydration at a depth of 1.5 mm are also shown to significantly reduce ($p<0.05$) interfacial micromotion induced stresses on the shank. The comparative measurements at depths of 1.0 mm and 1.5 mm for both non-compliant, bare silicon and PVAc –coated silicon shanks were not significantly different.

4. DISCUSSION

The mechanical mismatch between brain tissue and implants has long been hypothesized to induce strain in brain tissue in the immediate vicinity of the implants exacerbating glial scarring and neurodegeneration at the interface, leading to progressive signal loss over long implantation periods. Typical materials used for electrically active implants and electrodes include tungsten (400 GPa elastic modulus), stainless steel (200 GPa), and silicon (180–200 GPa) [50, 51]. Comparatively, the elastic modulus of brain tissue is at least 6 orders of magnitude less (3–15 kPa) [52] with individual neurons and astrocytes reportedly on the order of 1–100 Pa in elastic modulus [53]. In this study, we compared the mechanical behavior of the interfacial brain tissue in response to indentation and penetration by shanks of differing material properties. Here, non-compliant silicon (elastic modulus of ~200 GPa), PVAc-coated non-compliant, bare silicon (~49–78 GPa), and a novel, tunably compliant nanocomposite material in its 'stiff' state (5.2 GPa) and finally in its hydrated, 'soft' state (12 MPa) were tested. [42]

Despite the larger contact surface area of compliant nanocomposites, a key result of the experiments show that softer materials, especially nanocomposites, affect the viscoelastic properties of brain tissue. Based on viscoelastic models of interfacial brain tissue (Fig.7), the 'soft' state of nanocomposite materials are shown to significantly retard the dynamic stress relaxation rate of the brain tissue. In addition, interfacial micromotion induced stress amplitudes are 30–50% lower with softer, compliant shanks compared to non-compliant, bare silicon shanks. This compares well with previously reported modeling results where a soft interface with an elastic modulus of 6 MPa was predicted to result in ~30–40% reduction in micromotion related stress/strain [54]. Interestingly, PVAc-coated silicon shanks (with an elastic modulus of 49–70 GPa) also exhibited significantly ($p<0.05$) lower micromotion induced stresses (by 37–40%) compared to bare silicon shanks. Clearly, alternative mechanisms, such as surface adhesion properties, must be considered to explain similar reduction in micromotion induced stresses by two materials (PVAc-coated silicon and nanocomposites) with significantly different elastic moduli. PVAc is known to have

strong tissue adhesive properties and therefore it may reduce the micromotion by strongly adhering to the tissue along all axial and normal/shear components, resulting in an extremely rigid, negative stiffness-like material [55].

In addition, since micromotion induces a continuous, periodic stress on the shank, the rate at which brain tissue relaxes may play a significant role under chronic implantation conditions. The mean short term time constant (τ_1) for PVAc-coated shanks is smaller (2.6 sec) than hydrated, 'soft' nanocomposites (5.6 sec), suggesting that the rate at which the brain tissue material returns to the original relaxed state is lower for the latter compared to the former. Since stress rate is directly related to strain rate, it is possible therefore that softer, compliant nanocomposite materials result in significantly lower strain rates on the brain tissue. There is evidence that high strain rates lead to increased injury in traumatic brain injury scenarios [56,57]. Further, *in vitro* tests by Karumbaiah *et al.* showed that an imposition of 1–3% strain on neuronal, astrocyte, and microglia did not cause immediate cell death as compared to results at 5% strain [58]. Further experiments conducted at 3% cyclical strain to emulate micromotion conditions at 1.3 Hz resulted cortical neuronal death after 4 hours of exposure, microglial cell death after 8 hours of exposure, and astrocyte death after 24 hours of exposure [58]. The estimated dynamic strain in the brain tissue in the current study based on measured micromotion stresses *in vivo* is 2.5–3.5% for bare silicon shanks (Fig.8). Comparatively, PVAc-coated shanks and soft nanocomposite shanks imposed less strain on the interfacial tissue (up to 1.5%) which when compared to work by Karumbaiah *et al* suggest that the above shanks are expected to cause minimal cell death under long-term implantation conditions. Recent histological evidence indicate that the softer, nanocomposite implants reduced infiltration of IgG into the brain tissue as well as microglial activation and neurodegeneration compared to the much stiffer PVAc-coated implants at chronic time points ($p < 0.001$) [42] However, in the context of the acute measurements made here, it is interesting to note that immunohistological analysis indicated no difference in neuroinflammatory events between the above two implants at short time points. The above data raises the interesting possibility that soft substrates may not reduce initial tissue injury from implantation but, as seen with the nanocomposites used here, result in significant reduction in both chronic strain rates and chronic strain levels (due to tissue micromotion) in the surrounding brain tissue. Therefore, at least two possible explanations exist for the discrepancy in the immediate reduction in tissue strain, but only a chronic effect on neuroinflammation. First, differences in the maturation of the glial scar seen in tissue surrounding compliant implants versus stiff implants [42] may result in increasing differences in the tissue strain. We have previously shown that steady state stresses remain as high as 10% (at 6–8 weeks) following the implantation of stainless steel microelectrodes [44]. Therefore, the long-term changes in the material properties of brain tissue at the implant-tissue interface, for soft/compliant implants, remain critical to our understanding for chronic microelectrode design. While beyond the scope of this study, tissue anisotropy in the healing cortex will need to accounted for in understanding the long-term changes in material properties. Nguyen et al. show using finite element modeling that the spatial variation in tissue strain extends upto 500 μm, which corresponds well to results from prior studies [44]. However, the complexity of the glial scar formation suggests that an isotropic assumption may not accurately represent the brain tissue material at the interface. Aside from anisotropy

from grey matter/ white matter transition areas and white matter tracts in the healing cortex, anisotropy is also expected to arise from the glial scar formation. Recent findings using diffusion tensor based imaging show that a cortical impact method that induced TBI in rodents led to significant and increased anisotropic contribution from reactive astrocytes in injured areas in the cortex [64]. Future mechanical models of brain tissue interfaces may benefit from incorporating data from diffusion tensor anisotropy and tractography for evaluation of novel electrode designs.

Additionally, while beyond the scope of this study, further understanding of whether negative-stiffness materials like PVAc [55] are a suitable class of coating materials for neural implants needs to be further elucidated. Second, it is equally as likely that different and distinct inflammatory pathways dominate various temporal aspects of tissue healing and remodeling following microelectrode implantation. Potter *et al.* has previously shown that curcumin-releasing softening polymer implants cause minimal microelectrodes-mediated neuroinflammation at acute time points [59]. However, in their study, Potter *et al.* used poly(vinyl alcohol) as the polymer, which resulted in increased chronic inflammation. Therefore, future studies may also investigate the complementary mechanism of drug-releasing, strain-reducing poly(vinyl acetate) polymer microelectrodes (used here), at acute and chronic time points. Further, the strains and strain rates estimated in this study for bare silicon is in the same range that was reported earlier [30] to cause cell death in a culture of neurons, astrocytes and microglia. However, the strains and strain rates estimated for the nanocomposite and PVAc-coated bare silicon electrodes in this study were significantly lower than those reported to cause cell death [30].

5. CONCLUSION

The mechanical properties of underlying substrate have been extensively shown to play a significant role in synaptic strength and neuronal function and morphology in numerous *in vitro* studies [60, 61]. Microglia and astrocytes, in addition to subcellular structures such as synapses in neurons have been demonstrated to be mechanosensitive [31] [62, 63]. Harris *et al.* [43] and Nguyen *et al.* [42] have shown that the presence of neuronal cell bodies increases near softer implants. Numerous modeling studies suggest that softer material impart less strain on tissue [42, 54]. In this study, nanocomposites and PVAc-coated, non-compliant materials were shown to impose the least strain on the interfacial brain tissue (~2–10 fold less) compared to non-compliant, bare silicon shanks. The micromotion induced stresses and viscoelastic parameters of the brain tissue derived surrounding bare silicon in this current study are comparable to literature values for brain tissue viscoelastic properties [44]. Although, the effect of soft interfaces on neural signal quality remains unknown, electrode designs in the future could benefit from soft interfaces to control and compensate for chronic mechanical stresses on the brain tissue.

Acknowledgments

# References

1. Schwartz AB. Cortical neural prosthetics. Annu Rev Neurosci. 2004; 27:487–507. [PubMed: 15217341]

2. Cogan SF. Neural stimulationrecording electrodes. Annu Rev Biomed Eng. 2008; 10:275–309. [PubMed: 18429704]

3. Anderson ML. Neural reuse: A fundamental organizational principle of the brain. Behav Brain Sci. 2010; 33:245–266. [PubMed: 20964882]

4. Oakes TR, Pizzagalli DA, Hendrick AM, Horras KA, Larson CL, Abercrombie HC, Schaefer SM, Koger JV, Davidson RJ. Functional coupling of simultaneous electricalmetabolic activity in the human brain. Hum Brain Mapp. Apr.2004 21:257–70. [PubMed: 15038007]

5. Carlson KS, Xia CZ, Wesson DW. EncodingRepresentation of Intranasal CO2 in the Mouse Olfactory Cortex. Journal of Neuroscience. 2013; 33:13873–13881. [PubMed: 23966706]

6. Duffau H. Brain mapping in tumors: Intraoperative or extraoperative? Epilepsia. 2013; 54:79–83. [PubMed: 24328878]

7. Simeral JD, Kim SP, Black MJ, Donoghue JP, Hochberg LR. Neural control of cursor trajectoryclick by a human with tetraplegia 1000 days after implant of an intracortical microelectrode array. Journal of Neural Engineering. 2011; 8:025027. [PubMed: 21436513]

8. Donoghue JP, Nurmikko A, Black M, Hochberg LR. Assistive technologyrobotic control using motor cortex ensemble-based neural interface systems in humans with tetraplegia. The Journal of Physiology. 2007; 579:603–611. [PubMed: 17272345]

9. Hochberg LR, Bacher D, Jarosiewicz B, Masse NY, Simeral JD, Vogel J, Haddadin S, Liu J, Cash SS, van der Smagt P, Donoghue JP. Reachgrasp by people with tetraplegia using a neurally controlled robotic arm. Nature. May 17.2012 485:372–5. [PubMed: 22596161]

10. Kim S-P, Simeral JD, Hochberg LR, Donoghue JP, Black MJ. Neural control of computer cursor velocity by decoding motor cortical spiking activity in humans with tetraplegia. Journal of Neural Engineering. 2008; 5:455–476. [PubMed: 19015583]

11. Liu X, McCreery DB, Bullara LA, Agnew WF. Evaluation of the stability of intracortical microelectrode arrays. IEEE Trans Neural Syst Rehabil Eng. Mar.2006 14:91–100. [PubMed: 16562636]

12. Ludwig KA, Uram JD, Yang J, Martin DC, Kipke DR. Chronic neural recordings using silicon microelectrode arrays electrochemically deposited with a poly(3,4-ethylenedioxythiophene) (PEDOT) film. Journal of Neural Engineering. 2006; 3:59–70. [PubMed: 16510943]

13. Burns BD, Stean JP, Webb AC. Recording for several days from single cortical neurons in completely unrestrained cats. Electroencephalogr Clin Neurophysiol. Mar.1974 36:314–8. [PubMed: 4130612]

14. Barrese JC, Rao N, Paroo K, Triebwasser C, Vargas-Irwin C, Franquemont L, Donoghue JP. Failure mode analysis of silicon-based intracortical microelectrode arrays in non-human primates. J Neural Eng. 2013; 10:066014. [PubMed: 24216311]

15. Prasad A, Xue QS, Dieme R, Sankar V, Mayrand RC, Nishida T, Streit WJ, Sanchez JC. Abiotic-biotic characterization of Pt/Ir microelectrode arrays in chronic implants. Front Neuroeng. 2014; 7:2. [PubMed: 24550823]

16. Prasad A, Xue Q-S, Sankar V, Nishida T, Shaw G, Streit WJ, Sanchez JC. Comprehensive characterizationfailure modes of tungsten microwire arrays in chronic neural implants. J Neural Eng. 2012; 9:056015. [PubMed: 23010756]

17. Biran R, Martin DC, Tresco PA. Neuronal cell loss accompanies the brain tissue response to chronically implanted silicon microelectrode arrays. Experimental Neurology. 2005; 195:115–126. [PubMed: 16045910]

18. Leung BK, Biran R, Underwood CJ, Tresco PA. Characterization of microglial attachmentcytokine release on biomaterials of differing surface chemistry. Biomaterials. Aug.2008 29:3289–97. [PubMed: 18485471]

19. McConnell GC, Rees HD, Levey AI, Gutekunst C-A, Gross RE, Bellamkonda RV. Implanted neural electrodes cause chronic, local inflammation that is correlated with local neurodegeneration. J Neural Eng. 2009; 6:056003. [PubMed: 19700815]

20. Saxena T, Karumbaiah L, Gaupp EA, Patkar R, Patil K, Betancur M, Stanley GB, Bellamkonda RV. The impact of chronic blood-brain barrier breach on intracortical electrode function. Biomaterials. 2013; 34:4703–4713. [PubMed: 23562053]

21. Goldstein SR, Salcman M. Mechanical factors in the design of chronic recording intracortical microelectrodes. IEEE Trans Biomed Eng. 1973; 20:260–9. [PubMed: 4196687]

22. Maynard EM, Fernandez E, Normann RA. A technique to prevent dural adhesions to chronically implanted microelectrode arrays. J Neurosci Methods. Apr 15.2000 97:93–101. [PubMed: 10788663]

23. Meyer, JU.; Edell, DJ.; Rutten, WLC.; Pine, J. Chronically Implantable Neural Information Transducers. 18th Annual International Conference of the IEEE Engineering in MedicineBiology Society; Amsterdam. 1996.

24. Kim YT, Hitchcock RW, Bridge MJ, Tresco PA. Chronic response of adult rat brain tissue to implants anchored to the skull. Biomaterials. May.2004 25:2229–37. [PubMed: 14741588]

25. Gilletti A, Muthuswamy J. Brain micromotion around implants in the rodent somatosensory cortex. Journal of Neural Engineering. 2006; 3:189–95. [PubMed: 16921202]

26. Potter KA, Buck AC, Self WK, Capadona JR. Stab injury device implantation within the brain results in inversely multiphasic neuroinflammatory neurodegenerative responses. J Neural Eng. 2012; 9:046020. [PubMed: 22832283]

27. Potter KA, Buck AC, Self WK, Callanan ME, Sunil S, Capadona JR. The effect of resveratrol on neurodegenerationblood brain barrier stability surrounding intracortical microelectrodes. Biomaterials. 2013; 34:7001–7015. [PubMed: 23791503]

28. Subbaroyan J, Martin DC, Kipke DR. A finite-element model of the mechanical effects of implantable microelectrodes in the cerebral cortex. Journal of Neural Engineering. 2005; 2:103–113. [PubMed: 16317234]

29. Cullen DK, Simon CM, LaPlaca MC. Strain rate-dependent induction of reactive astrogliosiscell death in three-dimensional neuronal-astrocytic co-cultures. Brain Res. Jul 16.2007 1158:103–15. [PubMed: 17555726]

30. Karumbaiah L, Norman SE, Rajan NB, Anand S, Saxena T, Betancur M, Patkar R, Bellamkonda RV. The upregulation of specific interleukin (IL) receptor antagonistsparadoxical enhancement of neuronal apoptosis due to electrode induced strainbrain micromotion. Biomaterials. 2012; 33:5983–5996. [PubMed: 22681976]

31. Moshayedi P, Ng G, Kwok JCF, Yeo GSH, Bryant CE, Fawcett JW, Franze K, Guck J. The relationship between glial cell mechanosensitivityforeign body reactions in the central nervous system. Biomaterials. 2014; 35:3919–3925. [PubMed: 24529901]

32. Biran R, Martin DC, Tresco PA. The brain tissue response to implanted silicon microelectrode arrays is increased when the device is tethered to the skull. J Biomed Mater Res A. 2007; 82:169–78. [PubMed: 17266019]

33. Subbaroyan J, Kipke DR. The role of flexible polymer interconnects in chronic tissue response induced by intracortical microelectrodes-a modelingan in vivo study. Conf Proc IEEE Eng Med Biol Soc. 2006:3588–91. [PubMed: 17947041]

34. Wester BA, Lee RH, LaPlaca MC. Developmentcharacterization of in vivo flexible electrodes compatible with large tissue displacements. J Neural Eng. Apr.2009 6:024002. [PubMed: 19255461]

35. Kozai TD, Kipke DR. Insertion shuttle with carboxyl terminated self-assembled monolayer coatings for implanting flexible polymer neural probes in the brain. J Neurosci Methods. 2009; 184:199–205. [PubMed: 19666051]

36. Kee-Keun L, et al. Polyimide-based intracortical neural implant with improved structural stiffness. Journal of MicromechanicsMicroengineering. 2004; 14:32.

37. He W, McConnell GC, Schneider TM, Bellamkonda RV. A Novel Anti-inflammatory Surface for Neural Electrodes. Advanced Materials. 2007; 19:3529–3533.

38. Biran R, Martin DC, Tresco PA. The brain tissue response to implanted silicon microelectrode arrays is increased when the device is tethered to the skull. Journal of Biomedical Materials Research. 2007; 82A:169–178. [PubMed: 17266019]

39. Ware T, Simon D, Arreaga-Salas DE, Reeder J, Rennaker R, Keefer EW, Voit W. Fabrication of responsive, softening neural interfaces. Advanced Functional Materials. 2012; 22:3470–3479.

40. Sharp AA, Panchawagh HV, Ortega A, Artale R, Richardson-Burns S, Finch DS, Gall K, Mahajan RL, Restrepo D. Toward a self-deploying shape memory polymer neuronal electrode. J Neural Eng. Dec.2006 3:L23–30. [PubMed: 17124327]

41. Langer R, Tirrell DA. Designing materials for biology medicine. Nature. 2004; 428:487–493. [PubMed: 15057821]

42. Nguyen JK, Park DJ, Skousen JL, Hess-Dunning AE, Tyler DJ, Rowan SJ, Weder C, Capadona JR. Mechanically-Compliant Intracortical Implants reduce the Neuroinflammatory Response. J Neural Eng. 2014; 11:056014. [PubMed: 25125443]

43. Harris JP, Capadona JR, Miller RH, Healy BC, Shanmuganathan K, Rowan SJ, Weder C, Tyler DJ. Mechanically adaptive intracortical implants improve the proximity of neuronal cell bodies. J Neural Eng. 2011; 8:066011. [PubMed: 22049097]

44. Sridharan A, Rajan S, Muthuswamy J. Long-term changes in the material properties of brain-tissue at the implant-tissue interface. J Neural Eng. 2013; 10:066001. [PubMed: 24099854]

45. Capadona JR, Shanmuganathan K, Tyler DJ, Rowan SJ, Weder C. Stimuli-responsive polymer nanocomposites inspired by the sea cucumber dermis. Science. 2008; 319:1370. [PubMed: 18323449]

46. Shanmuganathan K, Capadona JR, Rowan SJ, Weder C. Stimuli-responsive mechanically adaptive polymer nanocomposites. ACS Applied Materials & Interfaces. 2010; 2:165–174. [PubMed: 20305827]

47. Hess A, Capadona J, Shanmuganathan K, Hsu L, Rowan S, Weder C, Tyler D, Zorman C. Development of a stimuli-responsive polymer nanocomposite toward biologically-optimized, MEMS-based neural probes. Journal of Micromechanics Microengineering. 2011; 21:54009–17.

48. Das R, Gandhi D, Krishnan S, Saggere L, Rousche PJ. A Benchtop System to Assess Cortical Neural Interface Micromechanics. IEEE Trans Biomed Eng. 2007; 54:1089–1096. [PubMed: 17554827]

49. Gefen A, Gefen N, Zhu Q, Raghupathi R, Margulies SS. Age-dependent Changes in Material Properties of the Brain Braincase of the Rat. Journal of Neurotrauma. 2003; 20:1163–1177. [PubMed: 14651804]

50. Oliver WC, Pharr GM. An improved technique for determining hardness elastic modulus using load displacement sensing indentation techniques. Journal of Materials Research. 1992; 7:1564–1583.

51. Qian L, Li M, Zhou Z, Yang H, Shi X. Comparison of nano-indentation hardness to microhardness. Surface & Coatings Technology. 2005; 195:264–271.

52. Bensmaia SJ, Miller LE. Restoring sensorimotor function through intracortical interfaces: progress looming challenges. Nature Reviews Neuroscience. 2014; 15:313–325.

53. Lu Y-B, Franze J, Seifert G, Steinhauser C, Kirchhoff F, Wolburg H, Guck J, Janmey P, Wei E-Q, Kas J, Reichenbach A. Viscoelastic properties of individual glial cells neurons in the CNS. PNAS. 2006; 103:17759–17764. [PubMed: 17093050]

54. Polanco M, Yoon H, Bawab S. Micromotion-induced dynamic effects from a neuronal probe brain tissue interface. Nanosensors, Biosensors, Info-Tech Sensors Systems. 2013:869109–1.

55. Kucuk Y. Modeling Nonlinear Viscoelastic Nanoindentation of PVAc at Different Rates. Journal of Mechanical Engineering. 2013; 59:418–422.

56. LaPlaca MC, Cullen DK, McLoughli JJ, C RS II. High rate shear strain of three-dimensional neural cell cultures: A new in vitro traumatic brain injury model. J Biomech. 2005; 38:1093–1105. [PubMed: 15797591]

57. Ahmadzadeh H, Smith DH, Shenoy VB. Viscoelasticity of Tau Proteins Leads to Strain-Rate Dependent Breaking of Microtubules during Axonal Stretch Injury: Predictions from a Mathematical Model. Biophysical Journal. 2014; 106:1123–1133. [PubMed: 24606936]

58. Karumbaiah L, Norman SE, Rajan NB, Anand S, Saxena T, Betancur M, Patkar R, Bellamkonda RV. The upregulation of specific interleukin (IL) receptor antagonists paradoxical enhancement of neuronal apoptosis due to electrode induced strain brain micromotion. Biomaterials. 2012; 33:5983–96. [PubMed: 22681976]

59. Potter KA, Jorfi M, Householder KT, Foster EJ, Weder C, Capadona JR. Curcumin-releasing mechanically adaptive intracortical implants improve the proximal neuronal density blood-brain barrier stability. Acta Biomaterialia. 2014; 10:2209–2222. [PubMed: 24468582]

60. Previtera ML, Langhammer CG, Langranna NA, Firestein B. Regulation of dentrite arborization by substrate stiffness is mediated by glutamate receptors. Annals of Biomedical Engineering. 2010; 38:3733–3743. [PubMed: 20614247]

61. Georges PC, Miller WJ, Meaney DF, Sawyer ES, Janmey PA. Matrices with Compliance Comparable to that of Brain Tissue Select Neuronal over Glial Growth in Mixed Cortical Cultures. Biophysical Journal. 2006; 90:3012–3018. [PubMed: 16461391]

62. Paoletti P, Ascher P. Mechanosensitivity of NMDA Receptors in Cultured Mouse Central Neurons. Neuron. 1994; 13:645–655. [PubMed: 7917295]

63. Tyler WJ. The mechanobiology of brain function. Nature Reviews Neuroscience. 2012; 13:867–878.

64. Budde MD, Janes L, Gold E, Turtzo L, Frank JA. The contribution of gliosis to diffusion tensor anisotropy tractography following traumatic brain injury: validation in the rat using Fourier analysis of stained tissue sections. Brain. 2011; 134(Pt 8):2248–60. [PubMed: 21764818]
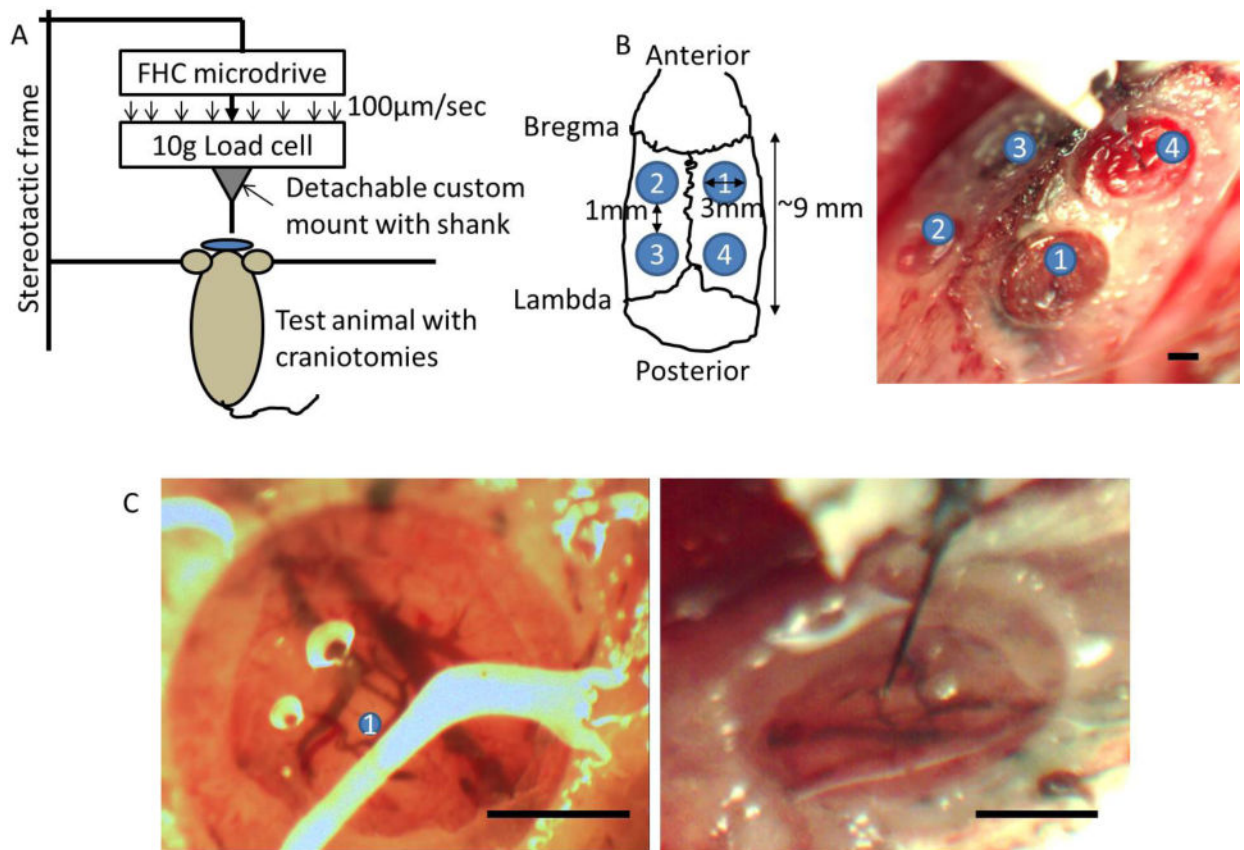
Fig.1.
(A) The experimental setup to measure force-displacement curves in brain tissue *in vivo* is illustrated. A load cell (10g, Futek, Irvine, CA) is attached to a stereotactic frame perpendicular to the craniotomy of an animal immobilized in the stereotactic frame. The attached shank (bare silicon, PVAc – coated silicon, or nanocomposite) with load cell is lowered into the craniotomy using an FHC microdrive (Bowdoin, ME) at 100 μm/sec. (B) Illustration shows the approximate placement of 4 craniotomies in the animal. Craniotomies were covered in gelfoam wetted with 0.9% saline to maintain hydration in between force measurements. In this representative picture, a PVAc-coated silicon shank is being placed at 1 mm depth in craniotomy #4. (C) Shown is a closeup of a craniotomy with dura (left) and after reflection of dura (right) showing minimal damage to vasculature. (1) marks the spot on brain tissue where minimal superficial vasculature is present and a bare silicon probe shank is inserted for force measurement. Note the silicon shank is in reality 90° (perpendicular) to the brain surface. The slanted view is due to the camera angle. Scale bar in (B) and (C) represents 1 mm.
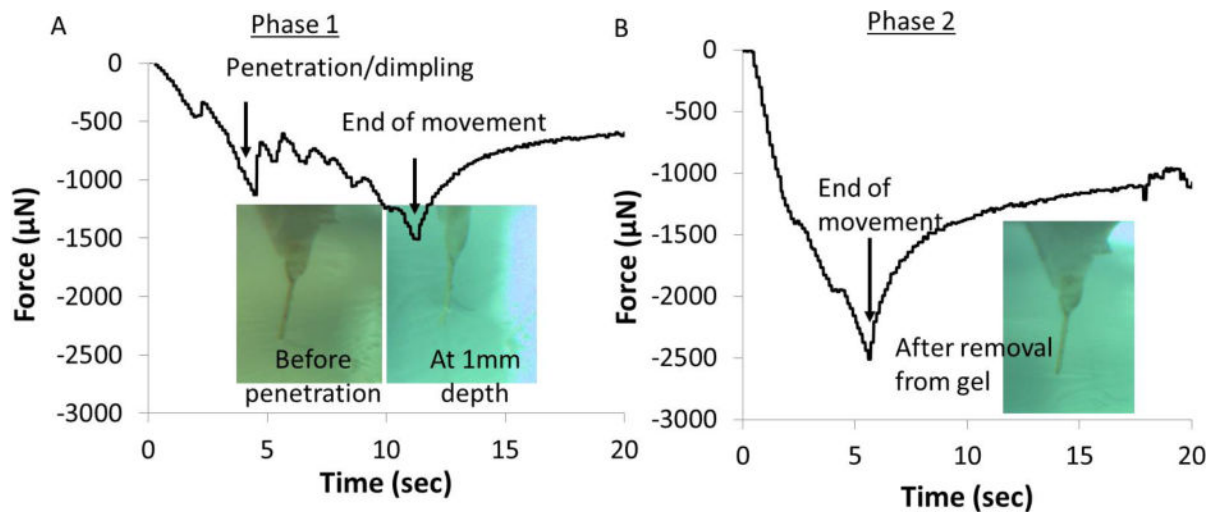
Fig.2.
Compliant nanocomposite shanks withstand indentation test. (A) In phase 1, the force-displacement curve of a compliant nanocomposite shank while it penetrates a 0.5% agarose gel mimic (elastic modulus of ~8kPa) at 100 μm/sec. First arrow at approximately 4.5 sec (450 μm depth) indicates penetration into the gel. Inset shows a closeup of nanocomposite shank prior to movement (left) and after placement at 1 mm depth (right). The nanocomposite shank is held stationary for 30 min prior to further movement in phase 2. (B) In phase 2, the force-displacement curve of the compliant nanocomposite shank as it moved an additional 500 μm in depth at the rate of 100 μm/sec is shown. Inset shows an intact nanocomposite shank after removal from gel, suggesting that a softened and more compliant shank maintains shape and form during the indentation test and after 30–45 min exposure to hydrated brain-like conditions.
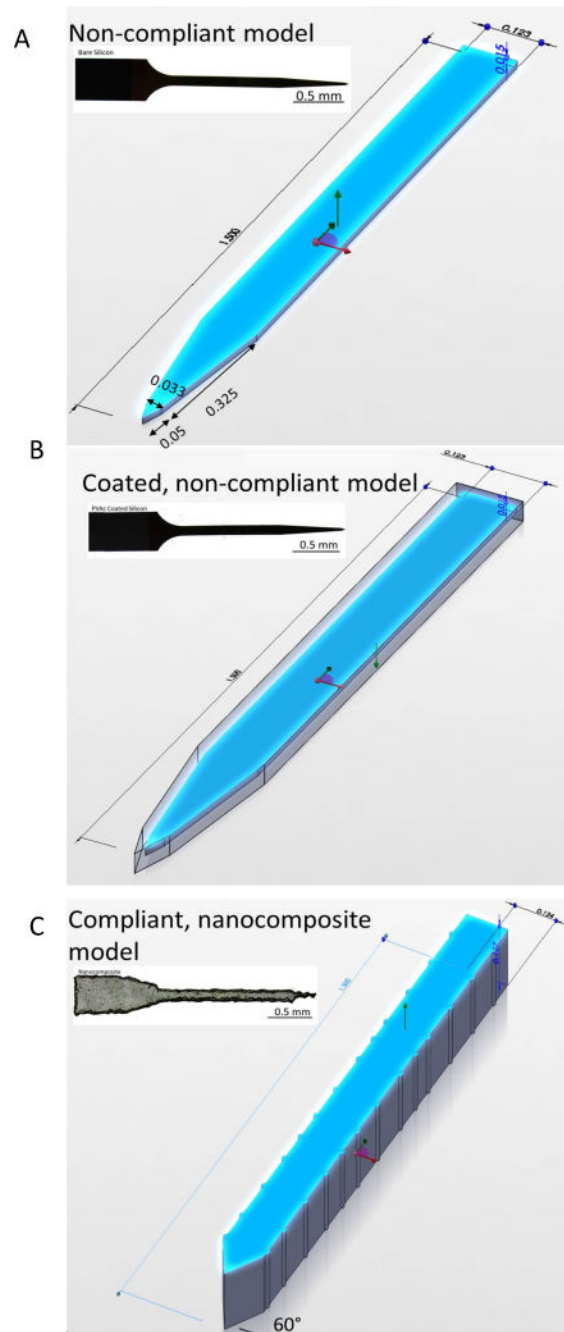
Fig.3.
For estimation of stress from complex geometries, CAD models in Solidworks™ were used
to derive contact surface areas with surrounding brain tissue for stress calculations for each
type of shank-(A) non-compliant bare silicon, (B) PVAc coated (15 μm thick) non-
compliant silicon, (C) compliant nanocomposite with an average roughness peak height (R_p)
of 7 μm occurring every ~130 μm along the shank (based on bright-field images). The units
for dimensions shown in the models are in (mm). Inset shows the bright-field image of each
representative shank.
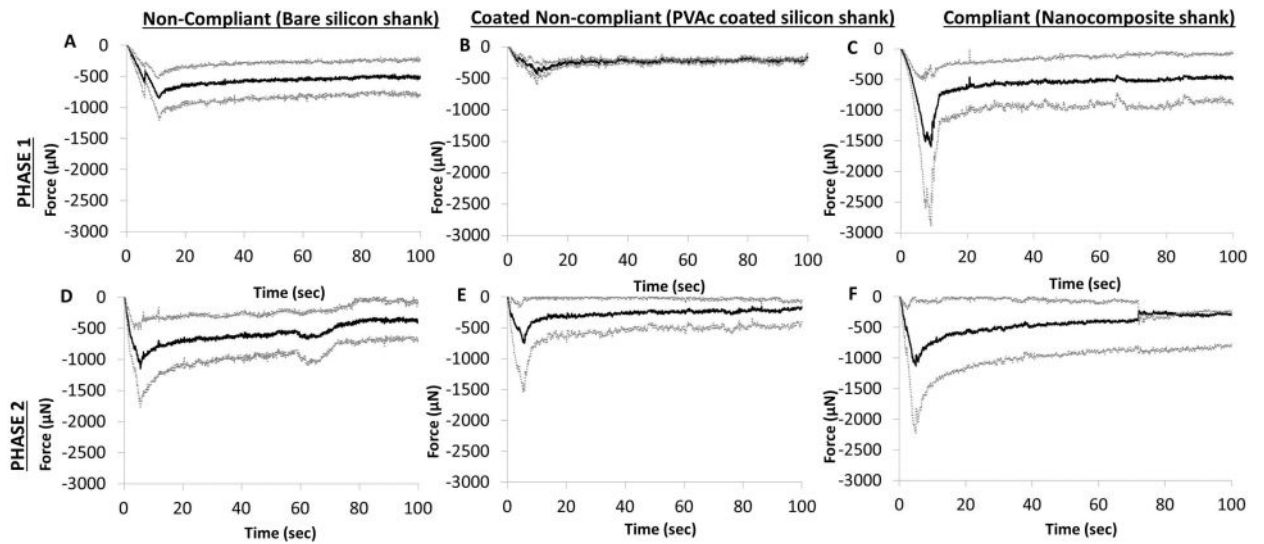
Fig.4.
Average force-displacement curves (black) ± standard deviation (gray)in (A) & (D) for bare silicon (non-compliant) shanks in phases 1 and 2 respectively (n=4 shanks), (B) & (E) for PVAc-coated silicon (coated, non-compliant) shanks in phases 1 and 2 respectively(n=3 shanks), and (C) & (F) for nanocomposite (compliant) shanks in phases 1 (n=6 shanks) and 2 respectively (n=5 shanks). One force curve was determined to be an outlier and was not included for nanocomposite phase 2 curves. Shanks are inserted at a speed of 100 μm/sec in both phase 1 (penetration phase (A–C)) and phase 2 (further downward movement by 0.5 mm (D–F)).
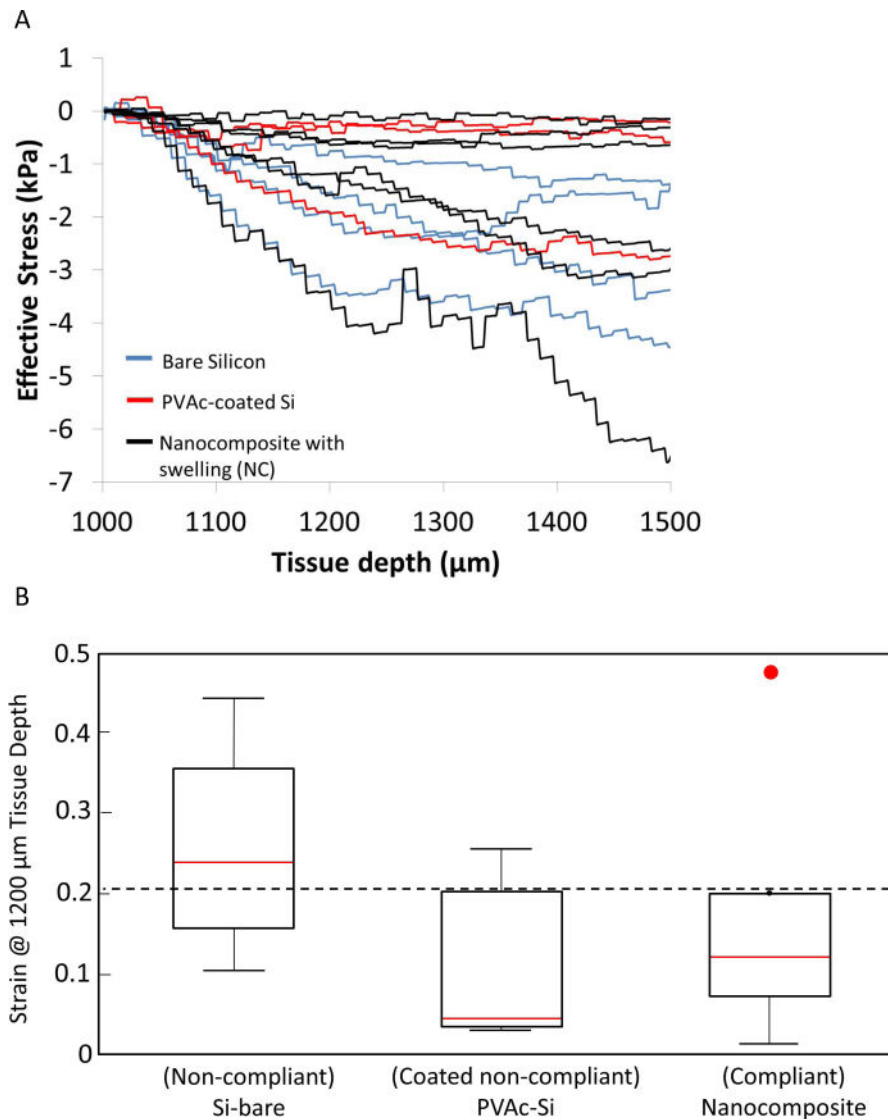
Fig.5.
(A) Dynamic stresses for non-compliant Si-bare (n=4 measurements), coated, non-compliant PVAc-coated Si (n=3 measurements), and compliant nanocomposite microelectrodes post-swelling (n=6 measurements) in <u>phase 2</u> as the microelectrodes were moved from 1.0 to 1.5 mm are shown as a function of tissue depth. A total of n=3 animals were used. Microelectrodes were moved at a constant speed of 100 μm/sec for a net change of 500 μm depth. (B) Strain was calculated using a linear model ($\sigma = E\varepsilon$), where σ =compressive stress, ε=compressive strain and the elastic modulus (E) of the brain is based on the median value for acute animals (7.5 kPa) [44]. Estimated strain which is expected to be maximum at a depth of 1200 μm corresponding to a net change of 200 μm from the beginning of microelectrode movement in phase 2) is plotted as a Tukey-Box plot for all three types of shanks (Si-bare (n=4 measurements), coated, non-compliant PVAc-coated Si (n=3 measurements), and compliant nanocomposite microelectrodes post-swelling (n=6 measurements). Dotted line highlights that 75% of strains in both PVAc-coated Si and
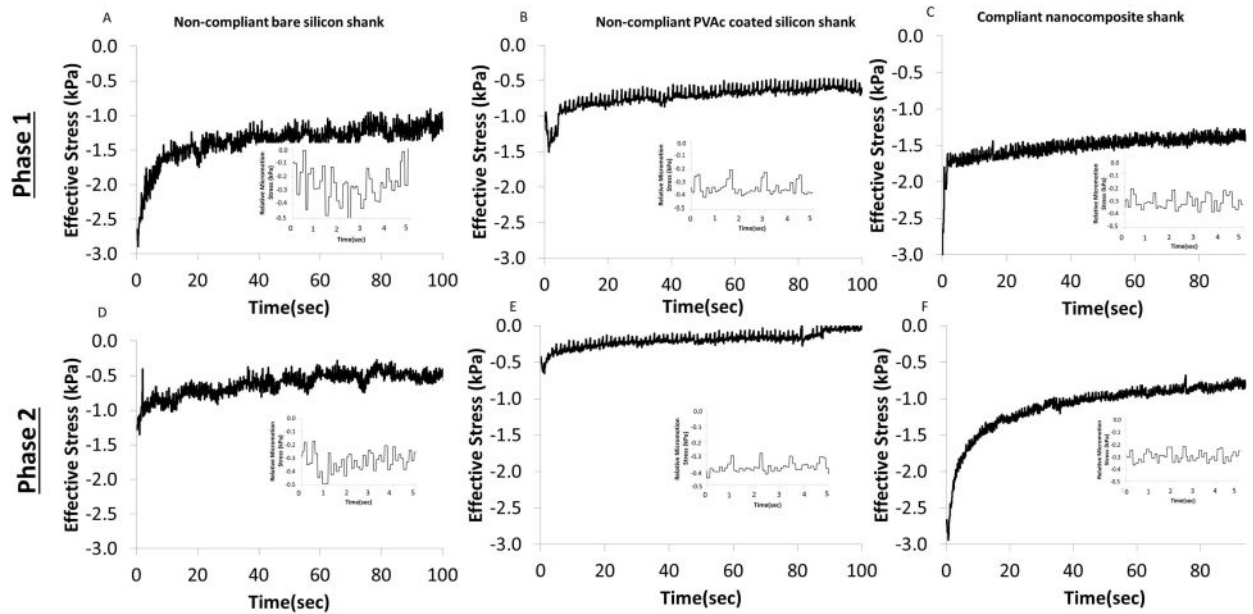
nanocomposite samples are well below the median strain value for bare Si. Red dot marks an outlier in nanocomposite samples.

Fig.6.
Representative relaxation stresses for non-compliant bare silicon (A,D), PVAc-coated non-compliant silicon (B,E), and compliant nanocomposite (C,F) microelectrodes. (A–C) represent relaxation stresses taken after microelectrode movement stops at a depth of 1.0 mm. (D–F) represent relaxation stresses taken after movement stops at a depth of 1.5 mm. Insets show representative micromotion related stresses due to breathing and vascular pulsatility over a 5 sec interval.
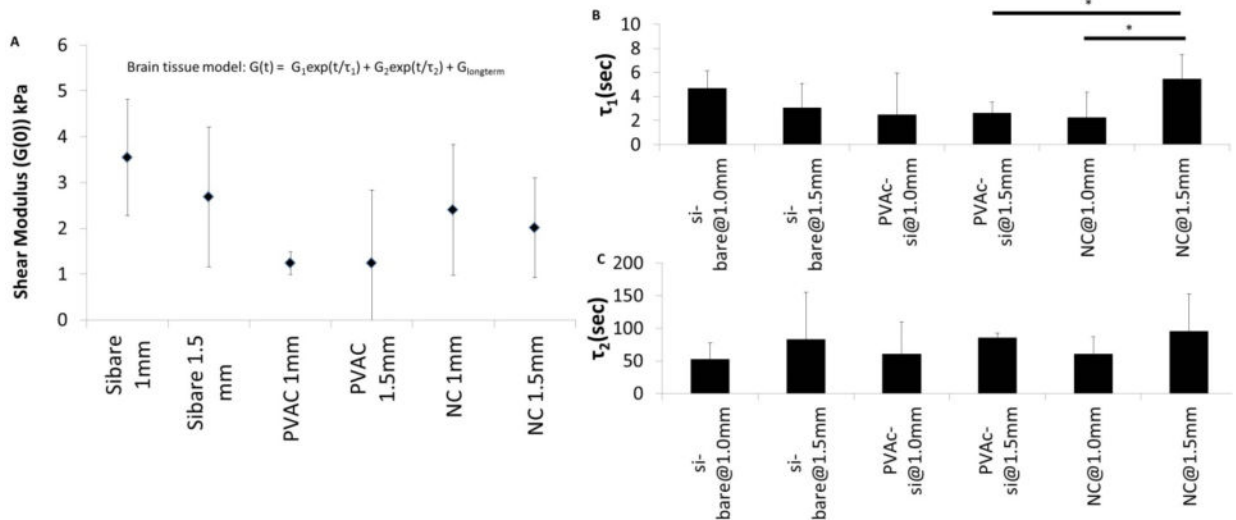
Fig.7.

A viscoelastic material model was derived from the relaxation stresses such as those in Fig. 6. Parameter estimation was performed for a 2nd order prony series model $G(t) = G_1 exp(t/\tau_1) + G_2 exp(t/\tau_2) + G_l$ where $G(t)$ is the shear stress over time (t), G_1, G_2, and G_l (sometimes refered to as G_∞) are stress materials parameters. τ_1 and τ_2 are time constants describing the short term and long-term relaxation of the brain tissue. (A) The instantaneous shear modulus $(G(0))$ which is calculated as: $G(0) = G_1 + G_2 + G_l$, shows no significant differences among the different samples, indicating acute brain material properties do not change due to interaction with shanks. (B) and (C) shows the comparative τ_1 and τ_2 time constants representative of the short-term and long-term relaxation properties of the brain tissue, respectively. In (B), τ_1 for the nanocomposite shank after hydration at 1.5 mm is significantly larger than those of the same shank before hydration at 1.0 mm and those corresponding to PVAc-coated silicon at 1.5 mm ($p < 0.05$ for both comparisons, indicated by *). (C) τ_2 shows no significant differences among the different samples. Significance was assessed using one-way ANOVA for G(0), τ_1 and τ_2 values, with α 0.05. Further tests among τ_1 values using Student's t-test using α=0.05 showed significant differences as indicated by the *.
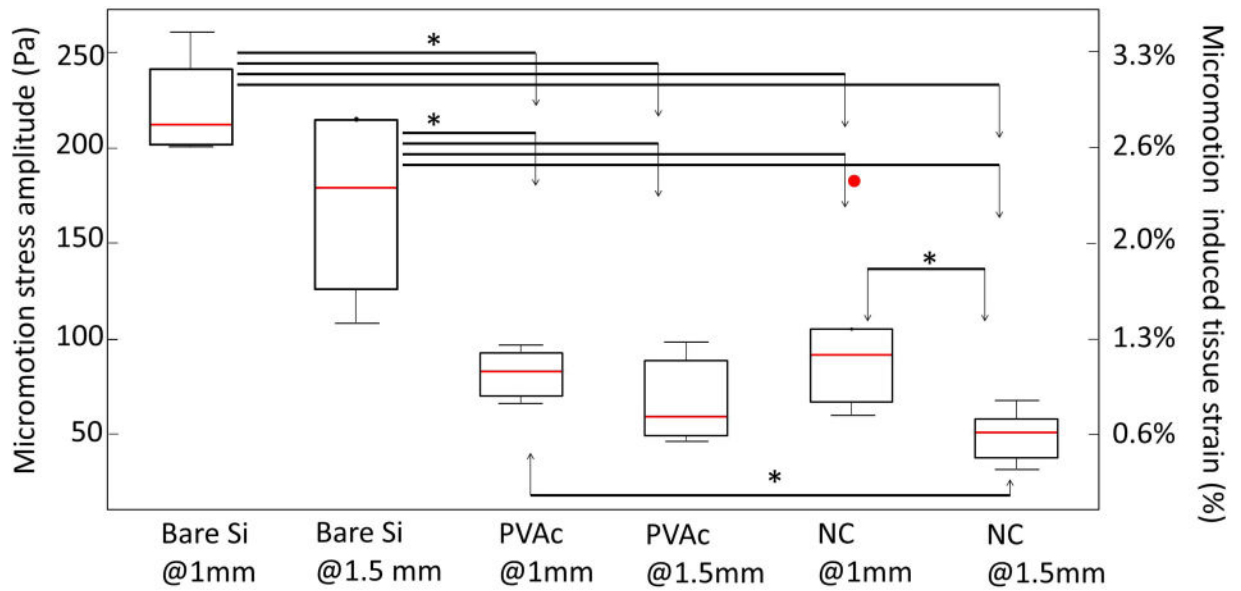
Fig.8.

Micromotion induced stress (y-axis on the left side) and strain (y-axis on the right side) amplitudes were pooled for non-compliant, bare silicon (n=4), PVAc-coated non-compliant silicon (n=3), and compliant nanocomposite (n=6) shanks from steady steady stresses at 1.0 mm and 1.5 mm tissue depth. Strain was estimated using a linear model (equation 1) as described in the methods section. * indicates a significant difference ($p<0.05$) based on Student's t-test (α=0.05). Red dot indicates an outlier.

Table 1

Contact surface areas of Si-Bare, PVAc, and NC based on SolidWorks CAD models

	@1.0 mm depth	@1.5 mm depth
Si-bare	2.36E-07m^2	3.74E-07m^2
PVAc-coated Si	3.44E-07 m^2	5.42E-07 m^2
NC	4.93E-07 m^2	8.27E-07m^2[**]

[**]
The nanocomposite samples were assumed to have an isotropic increase in volume of 11.2% after hydration (unpublished experimental data). This converged to a 6.5–7.0 μm increase in thickness in each dimension compared to the initially implanted shank.